# Hollow $Fe_2O_3$ nanotubes derived from metal-organic framework for enhanced lithium storage and dye adsorption

Chunyan Zhang[1] · Nianqiao Qin[1] · An Pan[1] · Jun Yuan[1] · Qianqian Liu[1] · Jiaqing Ren[1] · Zhong-hua Xue[1] · Mudassar Iqbal[2] · Yan Tian[1] · Fei Ke[1]

## Abstract

Hollow nanoparticles are of great interest in energy storage and environmental remediation due to their improved mass transfer ability and unique void space for confined pollutants. Herein, fabrication of highly efficient and recyclable hollow porous $\gamma$-$Fe_2O_3$ nanotubes is reported by direct thermolysis of MIL-88A (Fe) precursors. Metal-organic frameworks (MOFs) that served as the precursors of the hollow $\gamma$-$Fe_2O_3$ nanotubes were first synthesized by a facile hydrothermal method followed by a one-step annealing process. As a proof-of-concept application, the as-synthesized hollow porous $\gamma$-$Fe_2O_3$ nanotubes were used in the lithium-ion battery and dye adsorption, respectively. Taking advantage of the hollow porous structure, $\gamma$-$Fe_2O_3$ nanotubes exhibited excellent lithium-ion batteries performance (1559 mAh g$^{-1}$ at 100 mA g$^{-1}$) and corresponding long cycle life (1093 mAh g$^{-1}$ after 240 cycles at 100 mA g$^{-1}$). At the same time, maximum methyl orange (MO) uptake capacity for the as-prepared hollow $\gamma$-$Fe_2O_3$ was calculated to be as high as 63.17 mg g$^{-1}$. Moreover, this adsorbent also showed good reusability through the application of an external magnetic field, further highlighting the porous structure superiority of these hollow nanotubes. This proposed strategy could be extended to synthesize various hollow metal oxide porous nanoparticles with controllable structure, enhanced energy storage capacity and better environmental remediation performances.

**Keywords** Metal-organic frameworks · Porous nanostructure · Hollow nanotubes · Lithium-ion battery · Dye adsorption

## 1 Introduction

In the past decades, energy shortages and environmental pollution have sparked a potential global crisis concerning because of the rapid population growth and industrial development [1, 2]. Therefore, the development of green technologies for clean energy supplies and environmental remediation has become an important task. In recent years, lithium-ion batteries (LIBs) are considered as one of the prominent energy storage systems and broadly utilized in various electronic devices owing to their high energy density and long cycling life [3–6]. Due to its low cost, high electrical conductivity, and good chemical stability, graphite carbon is recognized as the leading electrode material for anodes of commercial LIBs [7]. However, the low capability of charge storage (theoretical capacity is only 372 mAh g$^{-1}$) limits its further applications. Thus, in order to meet the demands of ever-growing performance, searching for alternative anode materials has become an urgent task in building next-generation LIBs. On the other hand, clean water is extremely important for maintaining a high-quality life. Therefore, there is a crucial need for eco-friendly and economical methods to maintain water quality [8]. Dye pollution poses a great threat to human health and is considered as one of the main chemical pollutant affecting water quality. The removal of dyes from environment is considered a challenging task due to its stable structure [9]. In this regard, it is of great significance to develop multifunctional

Chunyan Zhang, Nianqiao Qin and An Pan contributed equally to this work.

✉ Zhong-hua Xue
zhonghua_xue@ahau.edu.cn

✉ Fei Ke
kefei@ahau.edu.cn

1 Department of Applied Chemistry and State Key Laboratory of Tea Plant Biology and Utilization, Anhui Agricultural University, Hefei 230036, People's Republic of China

2 Department of Agricultural Chemistry, The University of Agriculture, Peshawar 25130, Pakistan

nanomaterials which can show simultaneous superior lithium storage and dye adsorption.

$Fe_2O_3$ is a typically environment-friendly metal oxide anode material with various advantages of high theoretical capacity (ca.1006 mAh $g^{-1}$), low cost, and abundant resources, which has long been considered as a promising candidate for the new generation of high-efficiency anode materials [10–12]. However, larger volume changes and severe particle aggregation often occur during lithium ion insertion/extraction in the LIBs. This phenomenon would cause the transfer and diffusion performance of charge $Li^+$ to deteriorate, and the capacity to decay faster, which seriously limits the application of $Fe_2O_3$ in Li-ion batteries. To solve this problem, hollow porous nanostructures with porous outer shell minimize the transport length for both mass and Li-ion transport [13, 14]. Particularly, the interior space in the hollow structure cannot only provide additional active sites for Li-ion storage to increase the specific capacity, but also effectively relieve the structural strain induced by repeated Li-ion insertion/extraction processes and accommodate the possible volume variations [15]. Meanwhile, the hollow porous structure has a larger surface area, lower density, and higher load capacity,which is more conducive to the adsorption [16, 17].

Metal-organic framework (MOF) is usually composed of metal ions and organic ligands [18]. In recent years, MOF has gained significant importance due to its excellent characteristics such as high specific surface area, adjustable structure, and controllable pores [19, 20]. These frameworks have been widely used in adsorption [21], catalysis [22], and gas storage [23]. Recently, MOF is reported as a superior precursor/sacrificial template to synthesize hollow materials for energy storage and environment conservation [24, 25]. Zhu et al. synthesized hollow cobalt sulfide nanocrystals supported on graphene nanosheets by MOF as a template, and CoS@GN degraded BPA up to 100% in a wide range of pH [26]. Zhang et al. designed a hollow CeOx/CoP/NF nanocatalyst, and demonstrated excellent activities toward oxygen evolution reaction in anode and hydrogen evolution reaction in cathode with relatively low overpotential at 10 mA $cm^{-2}$ [27].

Herein, we develop a facile and green strategy to generate hollow porous $\gamma$-$Fe_2O_3$ nanotubes by direct thermolysis of MIL-88A (Fe) as both the precursor and the self-sacrificing template (Scheme 1). The as-obtained hollow porous $\gamma$-$Fe_2O_3$ nanotubes feature a high surface area, which guarantees good electrochemical performance and makes it more durable in long cycles. Accordingly, these characters endow the hollow $\gamma$-$Fe_2O_3$ nanotubes with superior electrochemical properties when used as anodes for LIBs. This can be attributed to the hollow porous structure which not only promotes the electron transport, but also effectively relieves the insertion/extraction caused by lithium ions changes in volume. Furthermore, as adsorbent, magnetic $\gamma$-$Fe_2O_3$ nanotubes exhibit excellent methyl orange (MO) adsorption performance followed by ease in their separation and reusability through the application of an external magnetic field.

## 2 Experimental section

### 2.1 Materials and methods

Ferric chloride hexahydrate ($FeCl_3 \cdot 6H_2O$), fumaric acid, ethanol, and methyl orange were purchased from Shanghai Chemical Reagent Co. Ltd., (P. R. China). All chemicals were of analytical grade and used without further purification. All solutions were freshly prepared before use with double distilled water.

The morphological information was collected by using field emission scanning electron microscope (FE-SEM, S4800, Hitachi, Japan) with an accelerating voltage of 10 kV and by transmission electron microscope (TEM, JEM model 100 SX, Japan) with an accelerating voltage of 300 kV. The crystallinities of the composites were measured by powder X-ray diffractometer (XRD, D/MAX-2500, RIGAKU, Japan) at 36 kV and 25 mA, using Cu target from 10 to 70°. Nitrogen adsorption-desorption isotherms were carried out with a Micromeritics TriStar II 3020 adsorption analyzer at 77 K. The X-ray photoelectron spectra (XPS) were obtained by using a Mg Kα radiation (1253.6 eV). UV-Vis absorption spectra were recorded on a Shimadzu UV-1800

**Scheme 1** Schematic illustration for the synthetic process of hollow porous $\gamma$-$Fe_2O_3$.
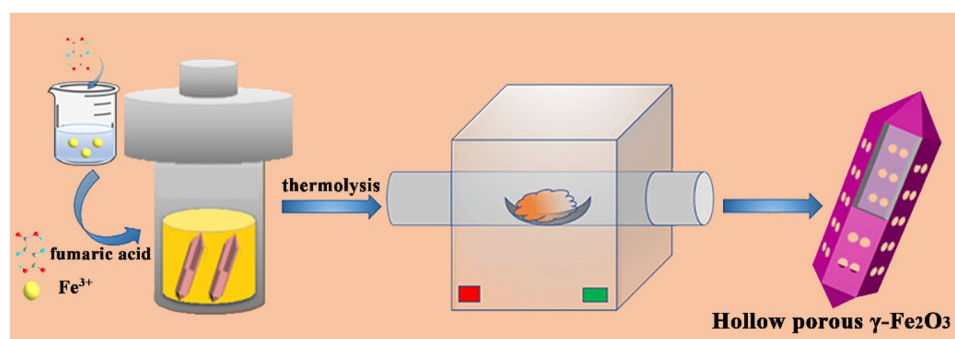
spectrophotometer. The TGA curve was obtained by MET-TLER TOLEDO thermogravimetric analyzer.

## 2.2 Synthesis of γ-Fe$_2$O$_3$

MIL-88A (Fe) was prepared according to the reported method [28]. Typically, a mixture of iron (III) chloride hexahydrate (FeCl$_3$·6H$_2$O, 1.6 g, 5.9 mmol), and fumaric acid (0.7 g, 6 mmol) was dissolved in the deionized water (30 mL) and sonicated for 20 min. Then the mixture was transferred into a 50 mL Teflon vessel autoclave, and placed under static conditions at 65 °C in an oven for 16 h and later centrifuged to collect a brown solid. The as-obtained sample was washed several times with EtOH and vacuum-dried at 80 °C overnight. The as-formed composite was placed in a ceramic boat and heated to 380 °C in the muffle furnace for 1 h under ambient atmosphere at a ramp rate of 10 °C min$^{-1}$. Upon naturally cooling, red-brown powder of the γ-Fe$_2$O$_3$ sample was collected and stored in an air tight vial for further use.

## 2.3 Electrochemical test

The electrochemical analysis was obtained with CR2016 coin type half cells that were assembled in an Ar-filled glove box. The working electrode was fabricated by mixing active materials, super-P carbon black and polyvinylidene fluoride (PVDF) in a weight ratio of 8:1:1 in N-methyl-2 pyrrolidinone (NMP) solvent. Copper foil, metallic lithium, and polyethylene film (Celgard, 2400) were employed as the collector, the counter electrode, and separator, respectively. A mixed solution containing LiPF$_6$ (1 M) and ethylene carbonate (EC)/dimethyl carbonate (DMC) (v:v = 1:1) was used as the electrolyte. The galvanostatic charge and discharge were performed on a battery testing system (CT-3008 W-5 V 10 mA, Neware Technology Co., Ltd., P. R. China) at various current densities between 0.01 and 3.0 V (vs. Li$^+$/Li). Cyclic voltammetry (CV) measurement was carried out on an electrochemical workstation (CHI660D, Shanghai CH instruments Co., Ltd., P. R. China) between 0.01 and 3.0 V (vs. Li$^+$/Li) at a scanning rate of 0.1 mV s$^{-1}$.

## 2.4 Methyl orange adsorption experiment

The adsorption capacity of as-synthesized γ-Fe$_2$O$_3$ adsorbent was calculated by conducting batch experiments of MO adsorption. For each experiment, 10 mg of γ-Fe$_2$O$_3$ adsorbent was added into 25 mL of MO solution that exhibited an initial concentration of 25 mg L$^{-1}$. The mixture was placed in a thermostatic shaker and shaken constantly at 150 rpm under room temperature. At regular intervals, 4 mL of supernatant was taken out, and used to detect MO concentration at 464 nm by using UV-Vis spectrophotometer. The adsorption

capacity and removal rate (%) of the sample for MO ($q_e$/mg g$^{-1}$) is calculated according to the following equations, respectively:

$$q_e = \frac{V(C_0 - C_e)}{m} \tag{1}$$

$$Removal\ (\%) = \frac{C_0 - C_e}{C_0} \times 100 \tag{2}$$

where $C_o$ and $C_e$ represent the initial and final concentrations of MO (mg L$^{-1}$), respectively; $V$ represents the volume of solution (L), and $m$ represents the mass of adsorbent (g) used.

## 2.5 Adsorption kinetics

For kinetic experiments, 25 mg of γ-Fe$_2$O$_3$ adsorbent was added separately into 25 mL of MO solution with various concentrations (6.25, 12.5, 25, 50, 100 and 200 mg L$^{-1}$). The reaction mixtures were placed in a thermostatic shaker and shaken constantly at 150 rpm at room temperature. The adsorption was periodically monitored using a UV-Vis spectrophotometer.

## 3 Results and discussion

### 3.1 Characterization of samples

The corresponding crystalline phase information and crystallographic structure of the as-obtained samples were characterized by XRD measurement. Figure 1a shows the typical XRD pattern of as-synthesized MIL-88A (Fe), in which all of the diffraction peaks are consistent with previously reported MIL-88A (Fe) [29]. For the obtained γ-Fe$_2$O$_3$ nanotubes, the identified diffraction peaks can be perfectly attributed to the Fe$_2$O$_3$ (JCPDS No. 33-0664) (Fig. 1b). Additionally, all of the diffraction peaks at 2θ = 24.14°, 33.18°, 35.68°, 40.94°, 49.54°, 54.12°, 57.6°, 62.40°, and 64.02° are indexed to (012), (104), (110), (113), (024), (116), (118), (214), and (300) crystal planes of γ-Fe$_2$O$_3$, respectively. No other phases or significant impurities were discerned in the XRD pattern except for the above component, indicating the high purity of porous γ-Fe$_2$O$_3$ nanotubes. Moreover, the chemical composition and valence states of the sample were further confirmed by X-ray photoelectron spectroscopy (XPS) measurement. As revealed by the survey spectrum of XPS analysis, Fig. 1c indicates that the sample is composed of Fe, O, and C elements. In the high-resolution spectrum (Fig. 1d), the binding energy peaks of Fe 2p located at around 710.9 eV and 724.4 eV can be ascribed

**Fig. 1** XRD patterns for (**a**) as-prepared MIL-88A (Fe) and (**b**) the calcined product, XPS spectrum (**c**) and high-resolution XPS spectrum of Fe 2p (**d**) of the as-synthesized $\gamma$-Fe$_2$O$_3$ nanotubes
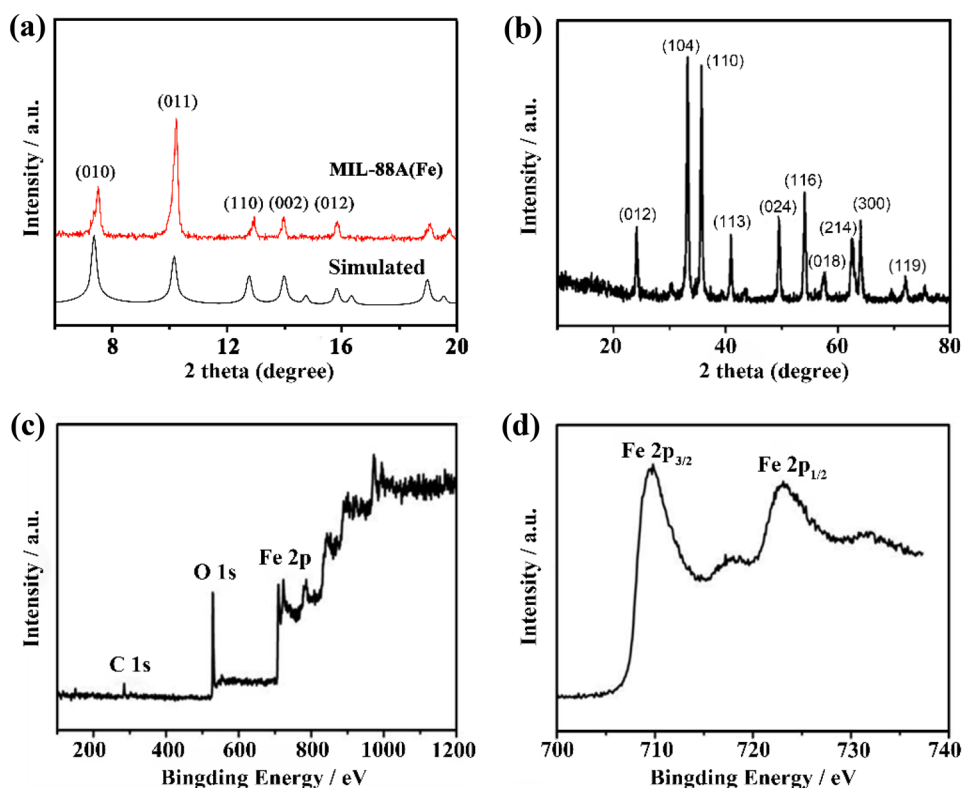


to Fe $2p_{3/2}$ and Fe $2p_{1/2}$ of Fe$^{3+}$, respectively, which are similar to the reported $\gamma$-Fe$_2$O$_3$ materials [30]. In addition, as can be seen from Fig. 1d that the peaks around at 717.8 and 733.9 eV, respectively, which are characteristic satellites of Fe$^{3+}$ in $\gamma$-Fe$_2$O$_3$ nanotubes. The morphologies and microstructures of the samples were characterized by

SEM and TEM images. As shown in Fig. 2a and c, the synthesis started with the formation of solid MIL-88A (Fe) pencil shape which displayed uniform and well-crystallized hexagonal with an average size of 7 µm in length and 1 µm in diameter. After being pyrolyzed in an air, the as-synthesized $\gamma$-Fe$_2$O$_3$ well maintains the pencil shape

**Fig. 2** SEM and TEM image for MIL-88A (Fe) (**a**, **c**) and hollow porous $\gamma$-Fe$_2$O$_3$ (**b**, **d**)
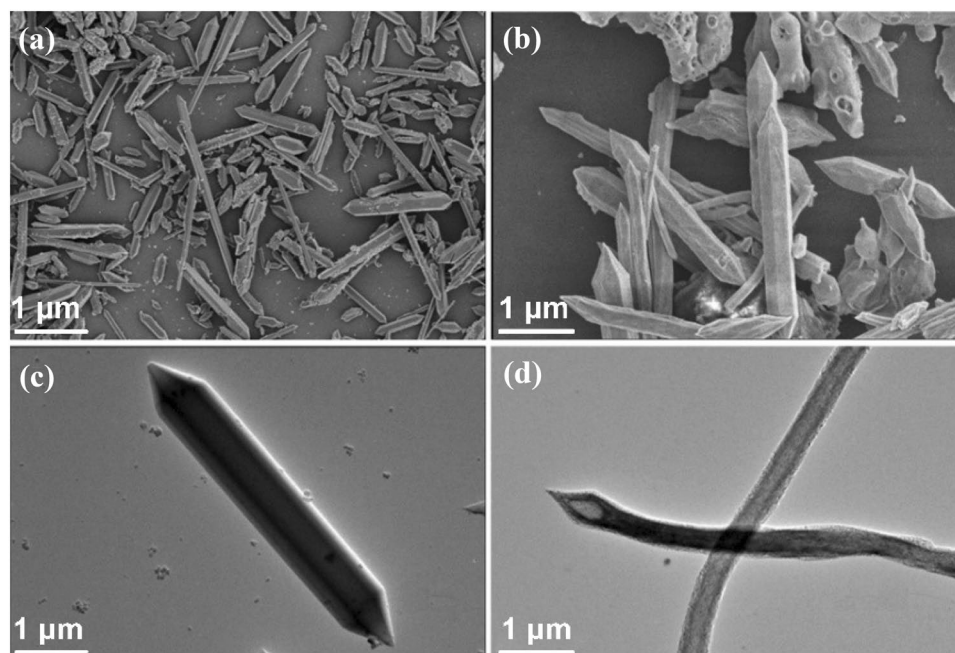
morphology of the pristine MIL-88A (Fe). Figure 2b represents the SEM images of as-synthesized γ-Fe₂O₃, unlike the solid MIL-88A (Fe), there is an extremely hollow morphology with openings on the wall of γ-Fe₂O₃ particles. The microstructure of the obtained γ-Fe₂O₃ was further analyzed by TEM image as shown in Fig. 2d, it clearly suggests the formation of a hollow structure with the diameter was around 400 nm,which is in agreement with the results revealed by the SEM image.

The specific surface area and pore structure of the as-prepared γ-Fe₂O₃ nanotubes were investigated by nitrogen adsorption-desorption isotherms at 77 K. The sample showed a type IV isotherm with hysteresis loop clearly observed at $P/P_0$ of 0.6-1 (Fig. 3a), suggesting the presence of mesopores. The Brunauer-Emmett-Teller (BET) surface area and pore volume of the products were calculated to be 101 m² g⁻¹ and 0.29 cm³ g⁻¹, respectively, demonstrating highly porous structures. Furthermore, the pore size distribution analysis using the Barrett-Joyner-Halenda (BJH) method reveals a broad range of pore diameter distribution from 5 to 25 nm. It is expected that this porous architecture can not only supply abundant active contact sites for the electron and Li⁺ conduction, but also help to buffer the volume expansion/contraction upon cycling, thus resulting in excellent LIBs performance. Figure 3b represents the TGA analysis of MIL-88A(Fe), revealing the weight loss at different temperatures. Obviously, the weight loss on the TGA curve is mainly divided into two parts. In the first part, the temperature drops at about 100 °C, which is mainly due to the volatilization of crystalline water in MIL-88A(Fe). The second weight loss was around 300-420 °C, mainly due to the decomposition of organic ligands. Refer to the relevant literature, we choose the appropriate temperature of 380 °C to calcined MIL-88A(Fe) into hollow γ-Fe₂O₃ [31].

## 3.2 Electrochemical performance of samples

The electrochemical performance of the samples as the anodes for LIBs was investigated. To deepen the understanding of the redox properties, cyclic voltammetry (CV) curves were performed in a voltage range of 0.01-3.0 V (Fig. 4a). The first cathodic curve exhibits a sharp peak around 0.7 V, being ascribed to the insertion of Li⁺ into the crystal structure with the reduction of $Fe^{3+}$ to $Fe^0$ and the formation of solid electrolyte interphase (SEI) films [32]. After the first cycle, the profiles of the CV curves become almost overlapped, indicating the electrochemical reactions are highly reversible in the following cycles. In the anodic scan, the broad anodic peak at ~1.7 V corresponds to the reversible oxidization of $Fe^0$ to $Fe^{3+}$. It is noteworthy that from the second cycle onwards the CV curves generally overlap, indicating a good reversibility of the redox reaction ($Fe^{3+}$ + $3e^-$ ↔ Fe) [33]. To further investigate the charge-discharge process of the samples, Fig. 4b displays the 1st, 2nd, 5th, 10th, and 50th discharge/charge profiles at a current rate of 100 mA g⁻¹ between 0.01 and 3.0 V (vs. Li⁺/Li). The voltage plateaus can be observed at ~0.7 V, which correspond well to the results of the cyclic voltammetry test. Figure 4c shows the charging/discharging behavior profiles of hollow porous γ-Fe₂O₃ from 1st cycle to 240th cycles at a current density of 100 mA g⁻¹ in a voltage range of 0.01~3.0 V. Initial discharge and charge capacities are 1559 and 1325 mAh g⁻¹, respectively, with an initial coulombic efficiency of about 85%. The loss of ~15% is mainly ascribed to the SEI layer formation, the irreversible conversion of γ-Fe₂O₃, and the incomplete extraction of Li ions from active materials. From the second cycle onwards, coulombic efficiency rapidly increases to about 95%. The hollow porous γ-Fe₂O₃ electrode exhibits remarkable cyclability, with a reversible capacity of about 1093 mAh g⁻¹ after 240 cycles. Figure 4d
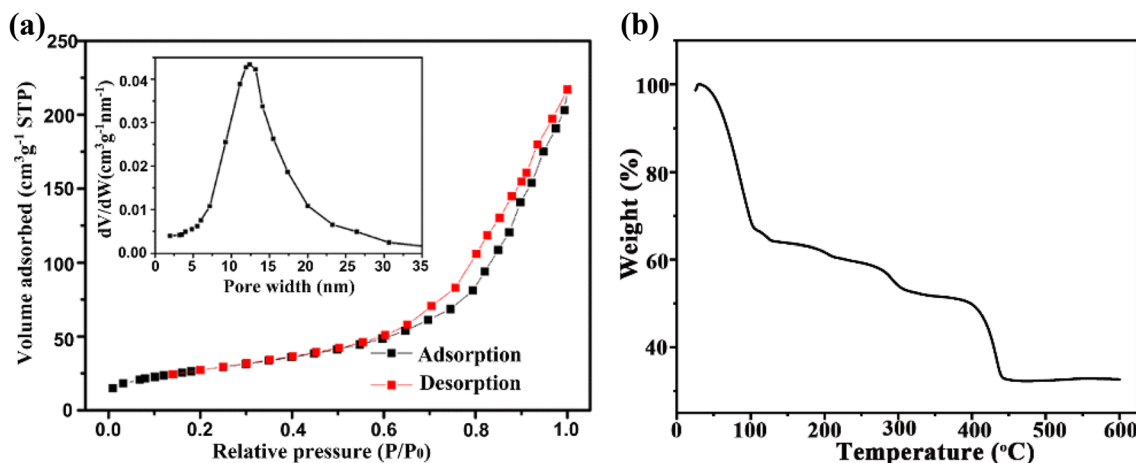


**Fig. 3** N₂ adsorption-desorption isotherms and pore-size distribution (inset) of the as-synthesized γ-Fe₂O₃(**a**), TGA curves of MIL-88A(Fe) (**b**)
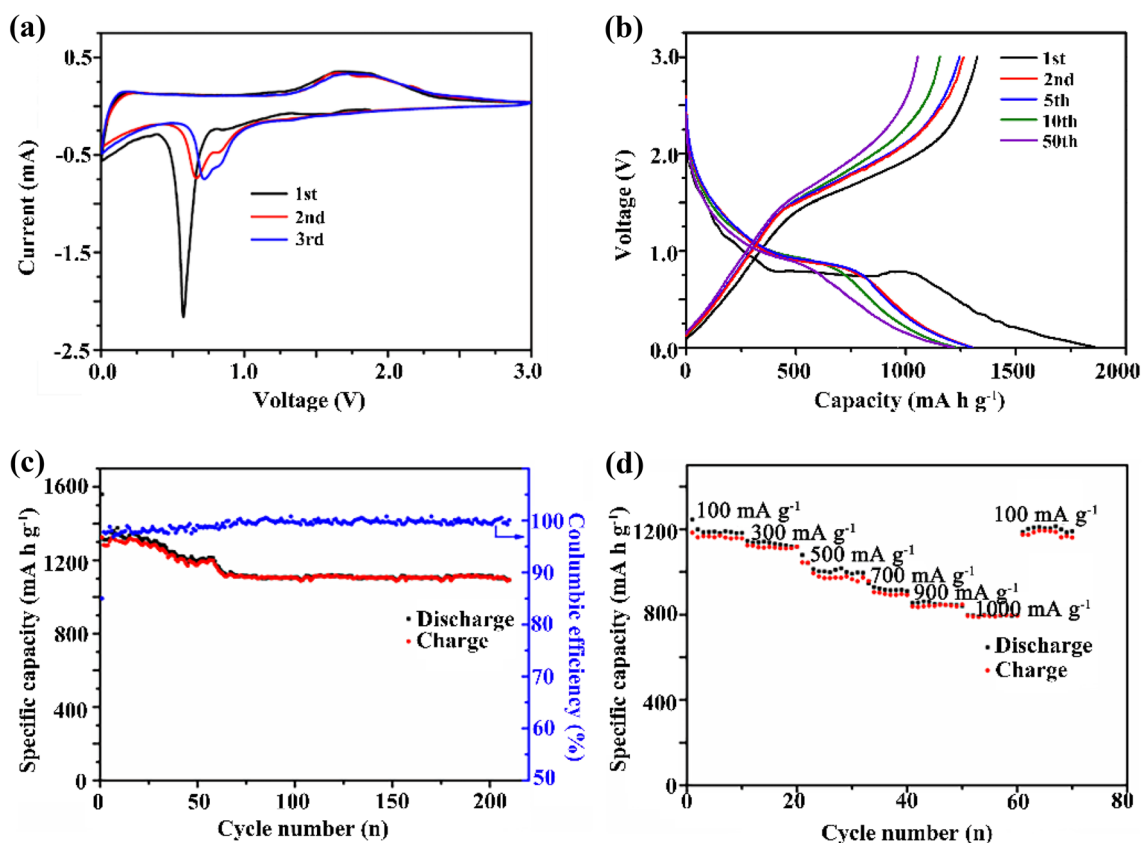
**Fig. 4** Electrochemical performances of γ-Fe₂O₃ as anode materials for LIBs: CV curves (**a**); Charge-discharge profiles at a current density of 100 mA g⁻¹ (**b**); Cycle performances and coulombic efficiency at 100 mA g⁻¹ (**c**); Rate capability at various current rates ranged from 100 to 1000 mA g⁻¹ as indicated (**d**)

shows the rate capability of the hollow porous γ-Fe₂O₃ at progressively increased current densities ranged from 100 to 300, 500, 700, 900 and 1000 mA g⁻¹, attractively, it displays capacities of 1187, 1139, 998, 914, 845 and 796 mAh g⁻¹ in sequence. More significantly, when the current density recovers to 100 mA g⁻¹ after cycling under high.

current densities, a reversible capacity near 1200 mAh g⁻¹ can be recovered again. These results indicate good stability of the hollow porous γ-Fe₂O₃ electrode after the high rate discharge-charge cycles.

## 3.3 Adsorption performance of samples

In order to understand the relationship between the maximum adsorption saturation of MO and the adsorption equilibration time, a kinetic study of adsorption was carried out. It is clearly evident from Fig. 5a that in the first 30 min, the adsorption of MO increased rapidly and later the adsorption rate slowed to reach an equilibrium within 7 h. The kinetics parameters were analyzed by the pseudo-second-order kinetic equation [34]:

$$\frac{t}{q_t} = \frac{1}{k_2 q_e^2} + \frac{t}{q_e} \tag{3}$$

Where $q_t$ and $q_e$ represent the amount of MO adsorbed at any time (t, min) and equilibrium (mg g⁻¹), respectively; $k_2$ is the rate constant of the pseudo-second-order adsorption (g mg⁻¹ min⁻¹). As depicted in Fig. 5b, the correlation factor of the fitting curve of the pseudo-second-order kinetic equation is 0.999, indicating that the removal of MO from the solution onto the hollow porous γ-Fe₂O₃ significantly follows the kinetic model. The kinetic rate constant ($k_2$) and the equilibrium adsorption capacity ($q_e$) values of γ-Fe₂O₃ were determined to be 0.023 g mg⁻¹ min⁻¹ and 17.51 mg g⁻¹, respectively.

The initial concentration of the analyte is one of the important factors of the adsorption capacity to the material. The hollow γ-Fe₂O₃ adsorbent was treated with a wide range of MO concentrations to study the maximum saturation adsorption capacity. The reactions were maintained for 7 h to ensure sufficient reaction time. As the initial concentration of MO in the solution increases, the adsorption capacity increases significantly and then tends to stabilize

**Fig. 5** Adsorption performances of γ-Fe₂O₃ as adsorbent: (**a**) effect of time on the concentration of MO at room temperature; (**b**) plots of pseudo-second-order kinetic of MO adsorption; (**c**) adsorption isotherms for the adsorption of MO; (**d**) the linear regression by fitting the data with Langmuir adsorption model
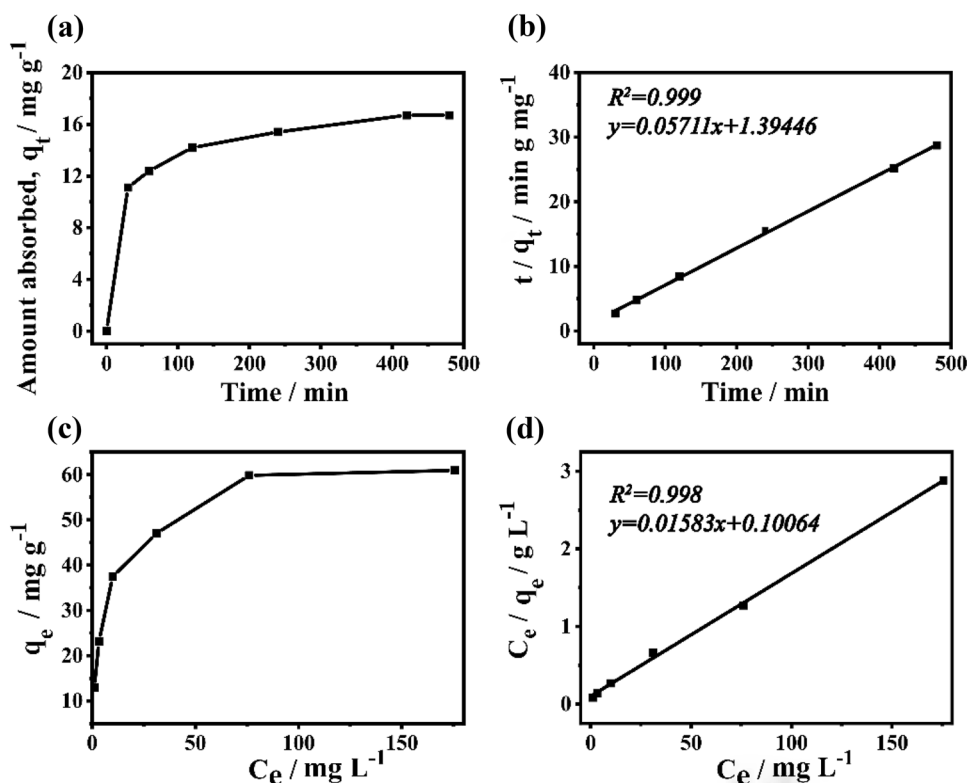


(Fig. 5c). When the initial concentration is sufficiently high (C = 100 mg L⁻¹), the active site of the adsorbent may be completely occupied, at which the adsorption reaches saturation and the adsorption capacity is the highest.

Besides, in order to have a better understanding of the adsorption capacity of γ-Fe₂O₃, we carried out the Langmuir model fitting on the adsorption data (Fig. 5d). The Langmuir equation (eq. 4) can be used to calculate the maximum saturated adsorption capacity of γ-Fe₂O₃ for MO [35]:

$$\frac{C_e}{q_e} = \frac{1}{q_m K_L} + \frac{C_e}{q_m} \tag{4}$$

Where $C_e$ represents the equilibrium concentration of remaining MO in the solution (mg L⁻¹), $q_m$ is the maximum adsorption capacity (mg g⁻¹), $q_e$ is the equilibrium adsorption capacity (mg g⁻¹) and $K_L$ is the Langmuir constant (L mg⁻¹). As depicted in Fig. 5d, the fitted line of $C_e$ and $C_e/q_e$ for MO adsorption at room temperature and the correlation factor of the curve is 0.998, demonstrating that the adsorption of MO conforms to the Langmuir adsorption model. At the same time, the results show that the maximum adsorption capacity of γ-Fe₂O₃ for MO is 63.17 mg g⁻¹. According to previous reports, Maguana et al. proved sugar scum is a suitable precursor for dye removal and the maximum adsorption capacity for MO removal was 15.24 mg g⁻¹ at the temperature 22 °C and pH 7.2 [36]. Masoud Shariati-Rad et al. prepared SiO₂-Fe₃O₄ magnetic

nanoparticles (SMNPs) for adsorption of MO and maximum adsorption was 53.19 mg g⁻¹ at pH 2.66 for 30 min [37]. Compared above, the adsorption capacity of γ-Fe₂O₃ for MO is 63 mg g⁻¹ at room temperature and neutral pH, so it has a certain value in practical applications.

The recyclability of the adsorbent is also important for practical applications. After completing the adsorption, γ-Fe₂O₃ adsorbents were easily collected by using a magnet, and then washed twice with distilled water and ethanol, dried in an oven at 70 °C for the next cycle. It is worth noting that, the adsorption efficiency of MO dropped only 7% (from 74% to 67%) for the hollow γ-Fe₂O₃ after five consecutive reuses (Fig. 6), indicating that the hollow porous γ-Fe₂O₃ possess excellent long-term stability and could be reused for a certain practical value.

## 4 Conclusions

In summary, we have successfully synthesized hollow porous γ-Fe₂O₃ nanotubes by a simple and effective pyrolysis strategy. The hollow porous nanotubes could provide rapid electron, ion, and mass transport. Owing to these unique properties, the as-synthesized γ-Fe₂O₃ nanotubes used as anode materials for LIB showed high reversible capacity and great cycling stability for more than 240 cycles. When employed as an adsorbent, hollow γ-Fe₂O₃ nanotubes not only showed effective adsorption capacity for MO, but
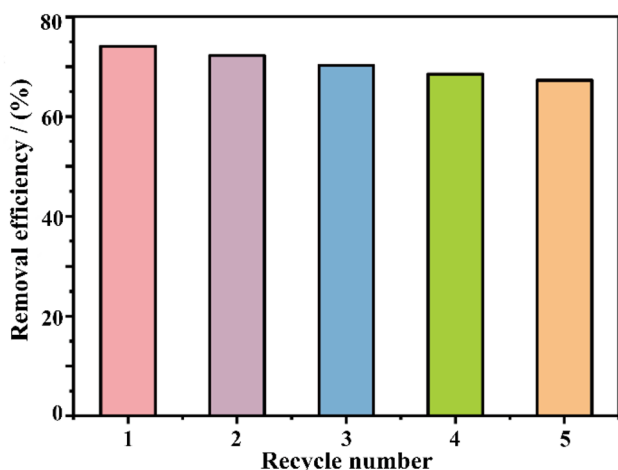
**Fig. 6** Recyclability experiments of hollow $\gamma$-$Fe_2O_3$ for the removal efficiency of MO

could also be recycled easily and reused by an external magnet. The straightforward method created here can be facilely extended to construct other functional materials with different components and unique properties which ensure their applications in the fields of catalysis, drug-delivery, biosensing, etc.

## Compliance with ethical standards

**Conflict of interest** The authors declare that they have no conflict of interest.

## References

1. D.K. Panchariya, R.K. Rai, E.A. Kumar, S.K. Singh, Core-shell zeolitic imidazolate frameworks for enhanced hydrogen storage. ACS Omega **3**(1), 167–175 (2018)
2. J. Saien, A. Azizi, F. Ghamari, Simultaneous photocatalytic reduction/degradation of divalent nickel/naphthalene pollutants in aqueous solutions. Water Sci. Technol. **79**(2), 240–250 (2019)
3. R. Kumar, S. Sahoo, E. Joanni, R.K. Singh, W.K. Tan, K.K. Kar, A. Matsuda, Recent progress in the synthesis of graphene and derived materials for next generation electrodes of high performance lithium ion batteries. Prog. Energ. Combust. **75**, 10786 (2019)
4. Y. Ma, Y. Chen, X.W. Zhou, H. Chen, Remaining useful life prediction of lithium-ion battery based on gauss-hermite particle filter. IEEE Trans. Control Syst. Technol. **27**(4), 1788–1795 (2019)
5. J.D. Huang, Z.X. Wei, J.Q. Liao, W. Ni, C.Y. Wang, J.M. Ma, Molybdenum and tungsten chalcogenides for lithium/sodium-ion batteries: Beyond $MoS_2$. J. Energy Chem. **33**, 100–124 (2019)
6. Q.B. Zhang, J. Liao, M. Liao, J.Y. Dai, H.L. Ge, T. Duan, W.T. Yao, One-dimensional $Fe_7S_8$@C nanorods as anode materials for high-rate and long-life lithium-ion batteries. Appl. Surf. Sci. **473**, 799–806 (2019)
7. W.J. He, T.F. Zhang, J.M. Jiang, C.L. Chen, Y.D. Zhang, N. Liu, H. Dou, X.G. Zhang, Efficient synthesis of N-doped $SiO_x$/C composite based on the defect-enriched graphite flake for lithium-ion battery. ACS Appl. Energ. Mater. **3**(5), 4394–4402 (2020)
8. M.A. Oturan, J.J. Aaron, Advanced oxidation processes in water/wastewater treatment: Principles and applications. A review. Crit. Rev. Env. Sci. Tec. **44**(23), 2577–2641 (2014)
9. D. Pathania, G. Sharma, A. Kumar, M. Naushad, S. Kalia, A. Sharma, Z.A. Alothman, Combined sorptional-photocatalytic remediation of dyes by polyaniline Zr (IV) selenotungs to phosphate nanocomposite. Toxicol. Environ. Chem. **97**(5), 526–537 (2015)
10. M.T. Niu, F. Huang, L.F. Cui, P. Huang, Y.L. Yu, Y.S. Wang, Hydrothermal synthesis, structural characteristics, and enhanced photocatalysis of $SnO_2$/alpha-$Fe_2O_3$ semiconductor nanohetero structures. ACS Nano **4**(2), 681–688 (2010)
11. X.J. Zhu, Y.W. Zhu, S. Murali, M.D. Stollers, R.S. Ruoff, Nanostructured reduced graphene oxide/$Fe_2O_3$ composite as a high-performance anode material for lithium ion batteries. ACS Nano **5**(4), 3333–3338 (2011)
12. Y.S. Luo, J.S. Luo, J. Jiang, W.W. Zhou, H.P. Yang, X.Y. Qi, H. Zhang, H.J. Fan, D.Y.W. Yu, C.M. Li, T. Yu, Seed-assisted synthesis of highly ordered $TiO_2$@alpha-$Fe_2O_3$ core/shell arrays on carbon textiles for lithium-ion battery applications. Energy Environ. Sci. **5**(4), 6559–6566 (2012)
13. C.J. Niu, J.S. Meng, C.H. Han, K.N. Zhao, M.Y. Yan, L.Q. Mai, $VO_2$ nanowires assembled intohollow microspheres for high-rate and long-life lithium batteries. Nano Lett. **14**(5), 2873–2878 (2014)
14. X. Wang, X.L. Wu, Y.G. Guo, Y. Zhong, X. Cao, Y. Ma, J. Yao, Synthesis and lithium storage properties of $Co_3O_4$ nanosheet-assembled multishelled hollow spheres. Adv. Funct. Mater. **20**, 1680–1686 (2010)
15. G. Karunakaran, M. Kundu, S. Kumari, E. Kolesnikov, M.V. Gorshenkov, G. Maduraiveeran, M. Sasidharan, D. Kuznetsov, ZnO/$Cu_2MgO_3$ hollow porous nanocage: A new class of hybrid anode material for advanced lithium-ion batteries. J. Alloys Compd. **763**, 94–101 (2018)
16. H.K. Lee, S.W. Lee, Formation of hollow porous $TiO_2$ nanospheres via the encapsulation of $CO_2$ nanobubbles for high-performance adsorption and photocatalysis. Dalton Trans. **49**(24), 8274–8281 (2020)
17. Y. Wu, S.H. Hu, R. Xu, J.W. Wang, Z.Q. Peng, Q.B. Zhang, Y. Yu, Boosting potassium-ion battery performance by encapsulating red phosphorus in free-standing nitrogen-doped porous hollow carbon nanofibers. Nano Lett. **19**(2), 1351–1358 (2019)
18. J.R. Li, R.J. Kuppler, H.C. Zhou, Selective gas adsorption and separation in metal-organic frameworks. Chem. Soc. Rev. **38**(5), 1477–1504 (2009)
19. X.G. Wang, Q. Cheng, Y. Yu, X.Z. Zhang, Controlled nucleation and controlled growth for size predicable synthesis of nanoscale metal-organic frameworks (MOFs): A general and dcalable approach. Angew. Chem. Int. Ed. Engl. **57**(26), 7836–7840 (2018)
20. C.Z. Liao, M. Zhang, L.Y. Niu, Z.J. Zheng, F. Yan, Organic electrochemical transistors with graphene-modified gate electrodes for highly sensitive and selective dopamine sensors. J. Mater. Chem. B **2**(2), 191–200 (2014)
21. R. Wo, Q.L. Li, C. Zhu, Y. Zhang, G.F. Qiao, K.Y. Lei, P. Du, W. Jiang, Preparation and characterization of functionalized

metal-organic frameworks with core/shell magnetic particles ($Fe_3O_4$@$SiO_2$@MOFs) for removal of Congo red and methylene blue from water solution. J. Chem. Eng. Data **64**(6), 2455–2463 (2019)

22. R. Kaur, K. Vellingiri, K.H. Kim, A.K. Paul, A. Deep, Efficient photocatalytic degradation of rhodamine 6G with a quantum dot-metal organic framework nanocomposite. Chemosphere **154**, 620–627 (2016)

23. B. Boukoussa, F. Abidallah, Z. Abid, Z. Talha, N. Taybi, H.S. El Hadj, R. Ghezini, R. Hamacha, A. Bengueddach, Synthesis of polypyrrole/Fe-kanemite nanocomposite through in situ polymerization: Effect of iron exchange, acid treatment, and $CO_2$ adsorption properties. J. Mater. Sci. **52**(5), 2460–2472 (2017)

24. Y.Y. Lu, W.W. Zhan, Y. He, Y.T. Wang, X.J. Kong, Q. Kuang, Z.X. Xie, L.S. Zheng, MOF-templated synthesis of porous $Co_3O_4$ concave nanocubes with high specific surface area and their gas sensing properties. ACS Appl. Mater. Inter. **6**, 4186–4195 (2014)

25. J.W. Zhou, B. Wang, Emerging crystalline porous materials as a multifunctional platform for electrochemical energy storage. Chem. Soc. Rev. **46**(22), 6927–6945 (2017)

26. C.Q. Zhu, F.Q. Liu, C. Ling, H. Jiang, H.D. Wu, A.M. Li, Growth of graphene-supported hollow cobalt sulfide nanocrystals via MOF-templated ligand exchange as surface-bound radical sinks for highly efficient bisphenol A degradation. Appl. Catal. B-Environ. **242**, 238–248 (2019)

27. T. Zhang, X.X. Wu, Y.F. Fan, C.F. Shan, B.K. Wang, H.J. Xu, Y. Tang, Hollow $CeO_x$/CoP heterostructures using two-dimensional Co-MOF as template for efficient and stable electrocatalytic water splitting. Chemnanomat **6**(7), 1119–1126 (2020)

28. S.G. Khasevani, M.R. Gholami, Engineering a highly dispersed core@shell structure for efficient photocatalysis: A case study of ternary novel BiOI@MIL-88A(Fe)@g-$C_3N_4$ nanocomposite. Mater. Res. Bull. **106**, 93–102 (2018)

29. W.T. Xu, L. Ma, F. Ke, F.M. Peng, G.S. Xu, Y.H. Shen, J.F. Zhu, L.G. Qiu, Y.P. Yuan, Metal-organic frameworks MIL-88A hexagonal microrods as a new photocatalyst for efficient decolorization of methylene blue dye. Dalton Trans. **43**(9), 3792–3798 (2014)

30. Y. Li, Y.X. Zhou, X. Ma, H.L. Jiang, A metal-organic framework-templated synthesis of gamma-$Fe_2O_3$ nanoparticles encapsulated in porous carbon for efficient and chemoselective hydrogenation of nitro compounds. Chem. Commun. **52**(22), 4199–4202 (2016)

31. X.H. Cao, B. Zheng, X.H. Rui, W.H. Shi, Q.Y. Yan, H. Zhang, Metal oxide-coated three-dimensional graphene prepared by theUse of metal-organic frameworks as precursors. Angew. Chem. **126**(5), 1428–1433 (2014)

32. L. Li, J.B. Zhang, Q.S. Zhu, A novel fractional crystallization route to porous $TiO_2$-$Fe_2O_3$ composites: Large scale preparation and high performances as a photocatalyst and Li-ion battery anode. Dalton Trans. **45**(7), 2888–2896 (2016)

33. M. Li, C. Ma, Q.C. Zhu, S.M. Xu, X. Wei, Y.M. Wu, W.P. Tang, K.X. Wang, J.S. Chen, Well-ordered mesoporous $Fe_2O_3$/C composites as high performance anode materials for sodium-ion batteries. Dalton Trans. **46**(15), 5025–5032 (2017)

34. Q.S. Zhou, X.Y. Lin, B. Li, X.G. Luo, Fluoride adsorption from aqueous solution by aluminum alginate particles prepared via electrostatic spinning device. Chem. Eng. J. **256**, 306–315 (2014)

35. M. Mohapatra, K. Rout, P. Singh, S. Anand, S. Layek, H.C. Verma, B.K. Mishra, Fluoride adsorption studies on mixed-phase nano iron oxides prepared by surfactant mediation-precipitation technique. J. Hazard. Mater. **186**, 2011 (1751–1757)

36. Y.E. Maguana, N. Elhadiri, M. Benchanaa, R. Chikri, Adsorption thermodynamic and kinetic studies of methylorange onto sugar scum powder as a low-costinorganic adsorbent. J. CHEM-NY. **2020**, 1–10 (2020)

37. M. Shariati-Rad, M. Irandoust, S. Amri, M. Feyzi, F. Ja'fari, Magnetic solid phase adsorption, preconcentrationand determination of methyl orange in water samples using silicacoated magnetic nanoparticles and central composite design. Int. Nano. Lett. **4**(4), 91–101 (2014)